

# TopoGEN: topology-driven microstructure generation for in silico modeling of fiber network mechanics

Sara Cardona<sup>a</sup>, Mathias Peirlinck<sup>a,\*</sup>, Behrooz Fereidoonzezhad<sup>a,\*</sup>

<sup>a</sup>*Department of BioMechanical Engineering, Faculty of Mechanical Engineering,  
Delft University of Technology, the Netherlands*

---

## Abstract

The fields of mechanobiology and biomechanics are expanding our understanding of the complex behavior of soft biological tissues across multiple scales. Given the intricate connection between tissue microstructure and its macroscale mechanical behavior, unraveling this mechanistic relationship remains an ongoing challenge. Reconstituted fiber networks serve as valuable in vitro models to simplify the intricacy of in vivo systems for targeted investigations. Concurrently, advances in imaging enable microstructure visualization and, through generative pipelines, modeling as discrete element networks. These mesoscale ( $\mu\text{m}$ ) models provide insights into macroscale (mm) tissue behavior. However, a systematic study of how microstructural variations influence nonlinear tissue mechanics is still lacking. In this work, we develop an innovative framework to generate topologically-driven discrete fiber networks. Leveraging these networks, we generate models of interconnected load-bearing fiber components that exhibit softening under compression and are bending-resistant. By virtually replicating microstructural features of reconstituted collagen networks, such as fiber volume fractions and cross-link concentration, we evaluate the robustness of our simulations. Analyzing the nonlinear elastic behavior at varying polymerization temperatures, we find consistency between the in silico results and in vitro data from the literature. We extend our investigation beyond empirically measurable factors to explore microstructural effects at the single fiber level (i.e., fibril morphology and stiffness) that are challenging to investigate experimentally. TopoGEN allows us to mechanistically explore localized microstructural phenomena and relate microstructural changes to the bulk mechanical response of soft biological materials, hence providing an indispensable tool to further advance the fields of tissue biomechanics and engineering.

*Keywords:* microstructure, discrete fiber networks, representative volume element, fibrous materials, tissue biomechanics

---

\*Senior authors contributed equally. Correspondence:

*Email addresses:* `mplab-me@tudelft.nl` (Mathias Peirlinck), `b.fereidoonzezhad@tudelft.nl` (Behrooz Fereidoonzezhad)

## 1. Introduction

Microstructure drives function. In soft biological materials, the microstructure comprises a complex fibrous network known as the extracellular matrix. This intricate three-dimensional meshwork of fibers provides mechanical stability, elasticity, and strength and plays a crucial role in governing cellular processes (Dean et al., 2023). Cells interact with the extracellular matrix through mechanotransduction (Jansen et al., 2015), a process by which they sense environmental changes and convert mechanical impulses into biological responses (Fereidoonzehad et al., 2017; Peirlinck et al., 2019). The discipline of mechanobiology revolves around this dynamic feedback loop (Loerakker and Humphrey, 2022), which is regulated by highly localized micromechanical factors. A key challenge, shared across many engineering applications (Geers et al., 2010), is understanding the relationship between microstructural features (e.g., individual constituents and network properties) and macroscopic functions (e.g., mechanical behavior) of these networks. In the specific case of soft biological tissues, such as collagen network within the extracellular matrix, the primary challenge lies in the geometrical complexity and weakly connected microstructure that disrupts deformation affinity and gives rise to localized deformations (Mirzaali et al., 2020) highlighted in experimental studies (Cavinato et al., 2020). Therefore, in biological tissues, the relative spatial position of two neighboring particles after deformation cannot be fully described solely by their relative material position before deformation, and non-affinity must be considered. Addressing this challenge requires in-depth investigation of details associated with the individual constituents of the networks, such as fiber kinematics (Mahutga et al., 2023). Early computational models of soft biological tissues were predominantly continuum-based, drawing inspiration from histological data (Fung, 1967; Holzapfel et al., 2000; Gasser et al., 2005). These models rely on intuitive understanding, data availability, and a priori physical assumptions. Thus, they are descriptive tools of material mechanics but fall short in predicting complex loading scenarios or new materials behavior. Most notably, they fail to offer mechanistic insights into material behavior based on the structural information of their building blocks. Advancements in imaging techniques have led to more detailed representations of the extracellular space through network models. Such network models explicitly depict interconnected fibers as discrete networks (Lindström et al., 2010, 2013; Nan et al., 2018; Ban et al., 2019; Merson and Picu, 2020; Dalbosco et al., 2021; Eichinger et al., 2021a; Leng et al., 2021; Nikpasand et al., 2021; Filla et al., 2023; Kakaletsis et al., 2023; Mahutga et al., 2023; Wahlsten et al., 2023), establishing the connection between fiber mechanics and tissue behavior. On the experimental side, tissue engineers have developed quantitative techniques to precisely control the microstructure of reconstituted gels (e.g., by adjusting temperature or concentration) and assess their influence on mechanical response (Jansen et al., 2018). These analyses show that even small environmental changes can significantly impact microstructure. The bulk mechanical response results from multiple coexisting factors. Potential microstructural factors include fiber interconnectivity (i.e., the topology), fiber concentration in the sample volume, and their morphological properties. However, the interrelated and multiscale nature of these factors makes it challenging to disentangle the influence of individual variables on the overall mechanical behavior of the sample. Com-

putational models that adopt discrete fiber networks offer a highly valuable complementary approach to experiments, enabling a systematic examination of how specific microstructural features contribute to macroscopic properties. Most of the current *in silico* discrete fiber-based approaches are concentration-driven rather than topology-driven, matching fiber volume fractions from experiments. However, this approach overlooks the critical role of network topology and other microstructural parameters, such as the morphological characteristics of individual fiber constituents, in shaping mechanical behavior. Understanding the localized deformations and varied mechanical properties of these reconstituted biological networks is crucial for uncovering how mechanical cues regulate cellular behavior, influence tissue development, and contribute to disease progression (van Putten et al., 2016; Herum et al., 2017; Ayad et al., 2019; Buskermolen et al., 2020; Eichinger et al., 2021b; Espina et al., 2021; Kim et al., 2021; Atcha et al., 2023; Kumar et al., 2024; McEvoy and McNamara, 2024). Moreover, investigating how the microstructure, in terms of fiber and network properties, relates to the measured properties enables material behavior prediction and provides a solid foundation for designing engineered tissues with tailored macroscopic mechanics (Burla et al., 2019b, 2020).

In this study, we propose TopoGEN, a framework that integrates three-dimensional fiber network architectures with nonlinear finite element analysis to systematically explore the intricate governing structure-function relationships in soft tissues. Our framework features a generative pipeline to create topologically rich and microstructurally varying discrete fiber networks. We explore the effect of changing the microstructure on the overarching macroscale behavior and compare our results to experimentally studied reconstituted collagen networks, where similar topology variations are induced through temperature effects. To extend our analysis beyond experimentally measurable mesoscale parameters, such as concentration, we investigate complex microstructural effects, including the morphology and mechanics of individual fiber constituents, on the bulk mechanical response of soft biological materials.

## 2. Methods

### 2.1. Fiber network generation

We model biological networks as structures of connected fibers. To generate these networks, we partition a three-dimensional cubic domain into randomly seeded Voronoi polyhedrons and represent the fibers and cross-links as the tessellation and vertices, respectively. We then optimize this Voronoi-based fiber network using simulated annealing optimization technique (Yeong and Torquato, 1998; Lindström et al., 2010, 2013; Eichinger et al., 2021a) to match key topological features, i.e., average connectivity (valency) and fiber length distribution, to those of experimentally measured collagen fiber networks (Jansen et al., 2018). We set the to-be-minimized annealing system energy as the distance of the initial microstructural configuration from the target microstructural configuration achieved by gradually cooling the network and allowing it to transition to new neighboring microstructures. These neighboring states are generated by applying small random perturbations to the configuration at each iteration until the current and target distributions match. To address the challenge of directly comparing continuous length distributions to the log-normal target (Lindström

et al., 2010), we implement a binning algorithm that partitions fiber lengths into disjoint intervals ( $b$ ). Therefore, we assign each length observation ( $x$ ) to a specific interval and compute a discretized cost function expressing the difference between the binned distribution and the target. To this aim, we implement the Kullback–Leibler (KL) divergence (Kullback and Leibler, 1951), also known as relative entropy ( $\mathcal{D}_{KL}$ ), which is a non-symmetric measure quantifying how one probability distribution ( $p(x)$ ) diverges from a second reference probability ( $q(x)$ ) distribution:

$$\mathcal{D}_{KL}(p(x) \parallel q(x)) = \sum_{j=1}^b p(x_j) \log \left( \frac{p(x_j)}{q(x_j)} \right) \quad (1)$$

To transform our initial Voronoi-generated random fiber network into neighboring states at each simulated annealing iteration, we introduce two types of moves illustrated in Figure 1: dilutive transformations, which randomly remove fibers within the network and concentration-preserving transformations, which randomly move nodes within the cubic domain.

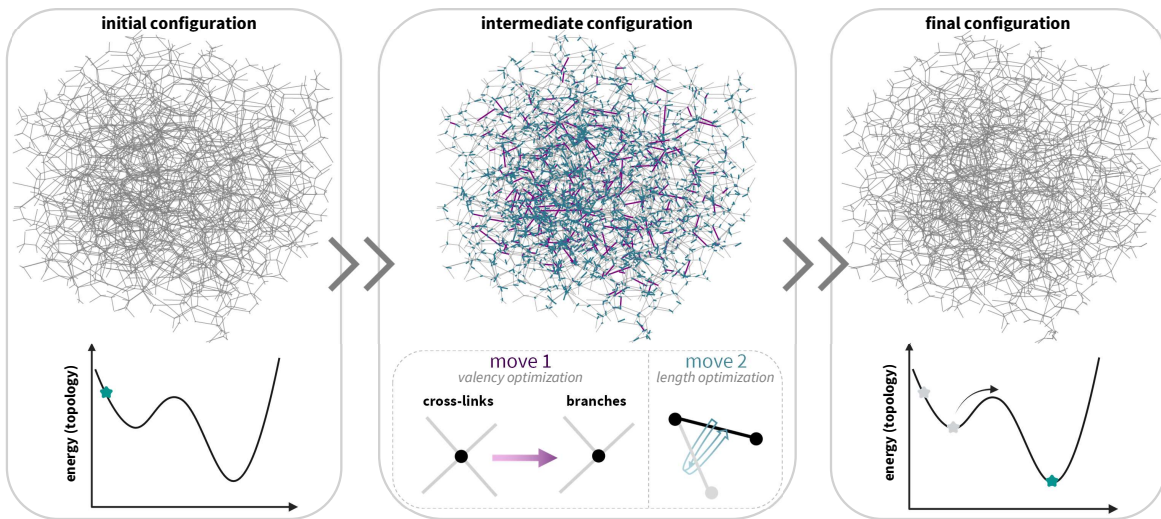


Figure 1: **Simulated annealing workflow.** Starting from an initial random configuration, the algorithm iteratively minimizes the system’s energy by removing fibers (move 1) or moving nodes (move 2) until the target distribution of valency and fiber length is achieved.

Here, we define cross-links as nodes with fourfold valency and branches as nodes with threefold valency. Starting from the fourfold valency typical of Voronoi networks, dilution allows branch formations until the target valency is reached. The Poisson length distribution used to generate the initial network results in a number of short fibers, which are inconsistent with experimentally measured target distribution. To address this, we assign higher removal probabilities to shorter edges during the dilutive transformations and iteratively adjust node position to match the log-normal distribution during the concentration-preserving transformations.

## 2.2. Mechanical equilibrium at the mesoscale

Modeling soft tissues at the level of individual fibers (microscale) or the level of discrete fiber networks (mesoscale) is computationally impractical for large volumes undergoing complex loading and boundary conditions. Instead of extending our discrete fiber network model to the entire tissue scale (macroscale), we focus on a representative volume element (RVE) large enough to statistically capture the mechanical properties of the microstructure yet small enough to reduce the computational cost. Within this mesoscale domain, we define a continuum-based constitutive behavior for each individual fiber in the network and apply macroscopic deformation gradients (i.e., tissue loading conditions) as boundary conditions. Solving this boundary value problem with the finite element method yields the macroscale’s local (i.e., for every finite element, at each integration point, within every time step, at each Newton iteration) constitutive law (Geers et al., 2010; Peirlinck et al., 2024). In this study, we use the commercial finite element analysis software Abaqus Dassault Systèmes Simulia Corp. (2024) to retrieve the numerical solution of the RVEs boundary value problem. The transition from the RVE to the full tissue scale is only admissible if the Hill-Mandel condition (Hill, 1963) is satisfied, ensuring that the potential energy remains consistent when passing from the meso- to the macroscale. This condition is ideally met with infinitely large RVEs; however, with finite-sized RVEs, the consistency requires careful handling of the boundary conditions and the RVE size. This can be achieved through three approaches: (1) enforcing zero microfluctuations throughout the RVE, i.e. coupling local RVE deformation affinely to the macroscale deformation gradient; (2) setting zero microfluctuations only at the boundary via uniform displacement boundary conditions while allowing internal nodes to deform non-affinely (i.e., with deviations from a direct one-to-one correspondence to the macroscale deformation gradient); or (3) imposing periodicity of the microfluctuation field at the boundary via periodic boundary conditions (PBCs) and allowing internal nodes to deform non-affinely. In this work, we adopt PBCs since they are known to estimate the overall material properties better than the other alternatives mentioned (Miehe and Koch, 2002; van der Sluis et al., 2000; Terada et al., 2000; Kanit et al., 2006; Perić et al., 2010) and lie closer to the effective properties compared to the upper and lower bounds defined by uniform displacement and traction boundary conditions. Another advantage of adopting PBCs is their ability to capture the effect of non-affinity on the RVE response by allowing internal nodes to move freely within our loosely connected networks. Given that biological networks are - in essence - not periodic structures, incorporating these PBCs is not a trivial task. Figure 2 highlights how we enforce periodicity at the boundary nodes while maintaining the internal microfluctuations. First, we randomly seed our RVE domain with  $N$  seeding points and generate 26 periodic replicas of this domain by offsetting the seeding points around the central domain (Figure 2, step 1). Next, we apply Voronoi tessellation using  $27 \times N$  points as seeding particles and extract the interconnected fibers from the skeletonized diagrams (Figure 2, step 2). We crop the larger network to the original cubic domain and assemble a periodic edge connectivity map between each boundary node and its periodic counterpart on the opposing edge (Figure 2, step 3). Finally, we implement PBCs by constraining the relative displacements of all node pairs, as defined in our assembled periodic boundary node connectivity table, to individual

dummy nodes. These dummy nodes, unattached to any fiber in the model, serve as reference points used in the nodal equations that impose the periodicity of the nodally paired loading conditions (Wu et al., 2014). In particular, at each individual dummy node, we enforce an affine macroscopic deformation gradient corresponding to the macroscopic RVE face deformation profile under study (e.g., uniaxial extension, biaxial extension, or shear, as illustrated in Figure 2, step 4). For each of these macroscopic deformation profiles, we introduce a linear interpolation map to constrain the boundary nodes to remain planar during shear or uni/biaxial tests.

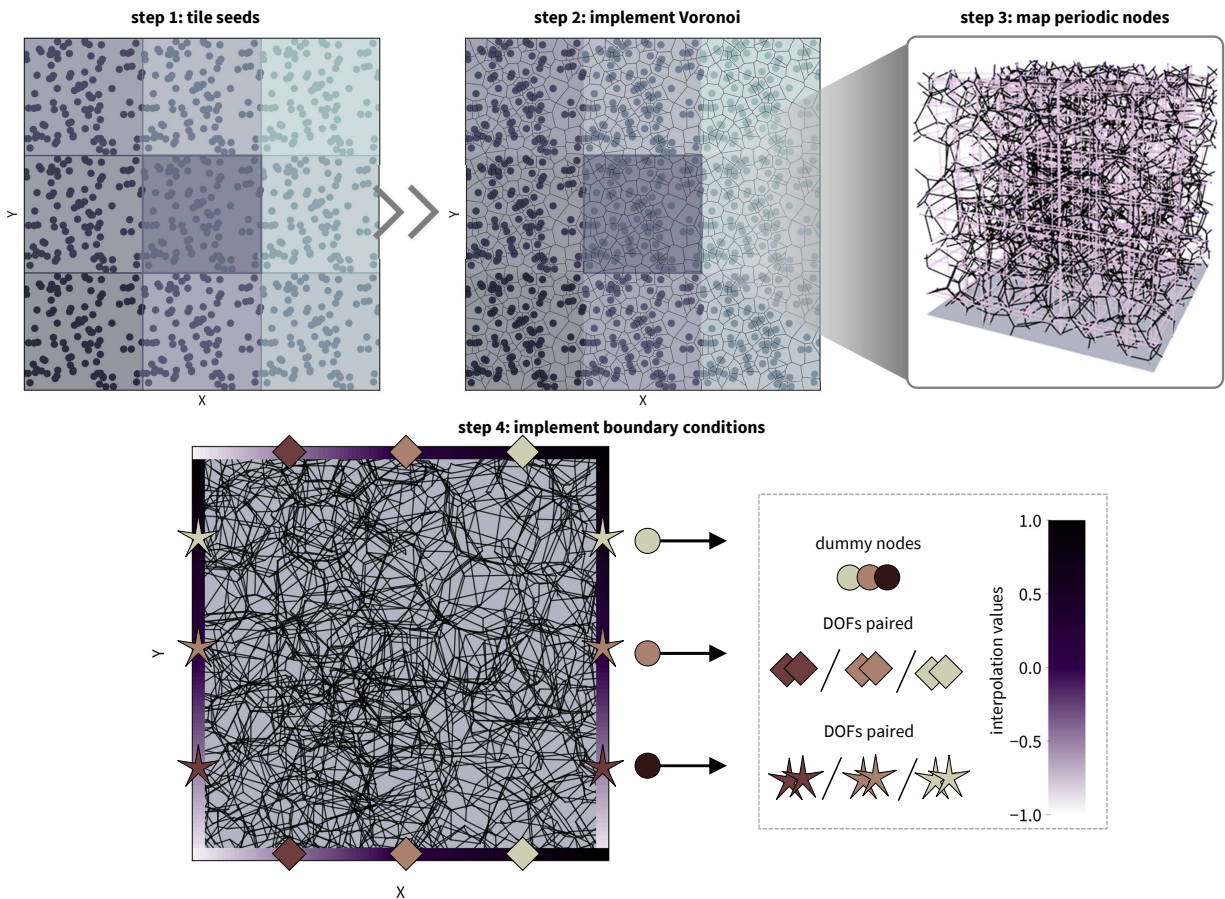


Figure 2: **Pipeline for generating periodic topology and applying periodic boundary conditions.** To achieve a periodic distribution of the boundary nodes, we tile the initial seeds in 26 replicas around the central domain (step 1) and tessellate the 3D space with a Voronoi diagram (step 2). Consequently, we map the nodes at the boundaries with their periodic counterpart (light purple dashed lines) and store the pairs to define the PBCs (step 3). Finally, we constraint the motion of node pairs located on opposing faces and ensure volume-preserving conditions by using an interpolation map on the free edges (step 4). For illustrative purposes, we show only tensile loading and implemented the conditions on the 2D case.

Focusing purely on elastic effects in this work, we assume fiber connections to be permanent, assuming no cross-link or branch breakage. We consider that the persistence length of

fibers, i.e., the characteristic length along the polymer chain over which its direction remains correlated before it starts to bend, is typically larger than the contour length. Therefore, the fibers are bending-stiff, and their thermal fluctuations can be neglected (Burla et al., 2019a). While the Euler-Bernoulli beam formulation could have been considered (Shahsavari and Picu, 2012), neglecting shear stiffness is mostly suited for fibers that are highly slender, i.e., with a cross-section-to-length ratio of less than 1:15. However, experiments in biological networks (e.g., collagen and fibrin) reveal a log-normal distribution of fiber lengths, which results in short fibers that violate this requirement (Lindström et al., 2010, 2013). Therefore, we model individual fiber mechanics using second-order Timoshenko shear-flexible beams, which are particularly suited for modeling biological networks (Shahsavari and Picu, 2013). We assume our fibers behave linearly elastic in both extension and compression, where we take into account fiber softening under compression by setting the compressive Young’s modulus to be a tenth of the tensile Young’s modulus (Notbohm et al., 2015). To incorporate this bilinear tension-compression asymmetry, we developed a custom user-defined field USDFLD subroutine that defines the fiber stiffness at each integration point based on the axial strain of the loaded beam. Upon solving the mechanical equilibrium of our topologically optimized RVEs under various periodic loading conditions, we obtain the reaction forces on our PBC-constrained faces. We use these reaction forces to compute a representative stress tensor across the entire discrete fiber network by calculating the first Piola–Kirchhoff stress tensor ( $\mathbf{P}$ ):

$$\mathbf{P} = \frac{1}{A_0} \sum_{i=1}^{N_i} \mathbf{f}_i. \quad (2)$$

where  $A_0$  denotes the initial surface of our cubic RVE,  $N_i$  are the dummy nodes, and  $\mathbf{f}_i$  represents the resulting external forces acting on these nodes.

### 2.3. Case study: rheological tests on collagen networks

We assess the role of microstructural features, including average valency, average fiber length and thickness, fiber elastic modulus, and network concentration on the differential elastic modulus, defined as the derivative of the stress with respect to the strain, as in Jansen et al. (2018). Our analysis employs the first Piola–Kirchhoff stress measure  $\mathbf{P}$  (Equation 2), which is first smoothed and then differentiated with respect to nominal strain to yield a nominal differential shear modulus. We compare our results with experimental data taken from Jansen et al. (2018), where the authors investigated (i) the nonlinear elastic behavior of rat tail collagen type I networks polymerized at different temperatures using a rheometer and (ii) network architecture features, including valency, fibril diameter and length through multiple imaging modalities. Briefly, Jansen and coauthors found that higher polymerization temperatures reduce the average valency and the fibril diameter (Table S.1). We virtually replicate these polymerized networks and their respective microstructural architectures by matching the in silico collagen concentration ( $\rho_c$ ) and the experimental values, as in Eichinger et al. (2021a), through:

$$\rho_c = \frac{L_{tot}\pi R_f^2}{V_{RVE}v_c}. \quad (3)$$

where  $R_f$  is the fiber radius,  $L_{tot}$  represents the sum of all individual fiber lengths,  $V_{RVE}$  denotes the volume of the RVE, and  $v_c$  is the specific volume of collagen fibers (Hulmes and Miller, 1979).

We create 40 x 40 x 40  $\mu\text{m}^3$  RVEs in which we model collagen fibrils as circular Timoshenko beams which - based on the respective polymerization temperature we aim to replicate - have diameters ranging from 160 nm to 300 nm and average lengths ranging from 1.6 to 3  $\mu\text{m}$  (Table S.1). We keep valency constant while varying the number of seeds within the fixed domain size and set the fiber’s tensile modulus equal to 700 MPa (Gacek et al. (2023)). We verify that these alterations consistently maintain the fiber radius-to-length ratio around  $10^{-3}$  (Licup et al. (2015)). We assume that concentration remains constant during polymerization.

### 3. Results

#### 3.1. Generation of microstructure-informed fiber networks

Figure 3 highlights the power of our TopoGEN pipeline to generate various topology-informed discrete fiber networks. Without loss of generality, we here leverage TopoGEN to generate collagen type I hydrogels representing the experimental in vitro networks generated by Jansen et al. (2018). Starting from random network initializations, we use simulated annealing to align the network architecture in terms of valency and edge length distributions, prioritized as key parameters for capturing isotropic network properties. To match the valency observed in self-assembled collagen type-I networks, where fibers form branches (valency 3) or cross-links (valency 4), we constrain our network to accept only these valency values. In particular, our generated discrete fiber network topologies replicate the observed decrease in average network valency associated with increasing temperatures. Therefore, as the temperature rises, inter-fiber interactions shift towards a prevalence of branch points over cross-links as can be seen from the decreasing valency in the top-left subplot of Figure 3. The length optimization follows a two-step process. First, we remove small, unrepresentative fiber segments during the valency optimization stage to ensure a physically meaningful network structure. To achieve this, we assign higher removal probabilities to shorter edges and iteratively optimize valency following this weighted edge removal approach. Next, we adjust node positions to align with the target length log-normal distribution using simulated annealing guided by the KL divergence metric. This metric demonstrates superior performance, achieving more significant improvement within runtimes comparable to a conventional technique, such as the Cramér-von Mises (CVM) test (Lindström et al. (2010, 2013); Eichinger et al. (2021a)). See Table S.2 for a detailed comparison across 20 independent tests of the performance metrics between the two methods. The average fiber length is optimized to match the experimentally measured fiber lengths observed across different temperatures (Table S.1), and the resulting log-normal distribution is depicted in the top-right subplot of Figure 3. In the bottom row of Figure 3, two-dimensional projections of our three-dimensional in silico



reconstructions are compared to high-resolution images of reconstituted collagen I network, taken from Jansen et al. (2018).

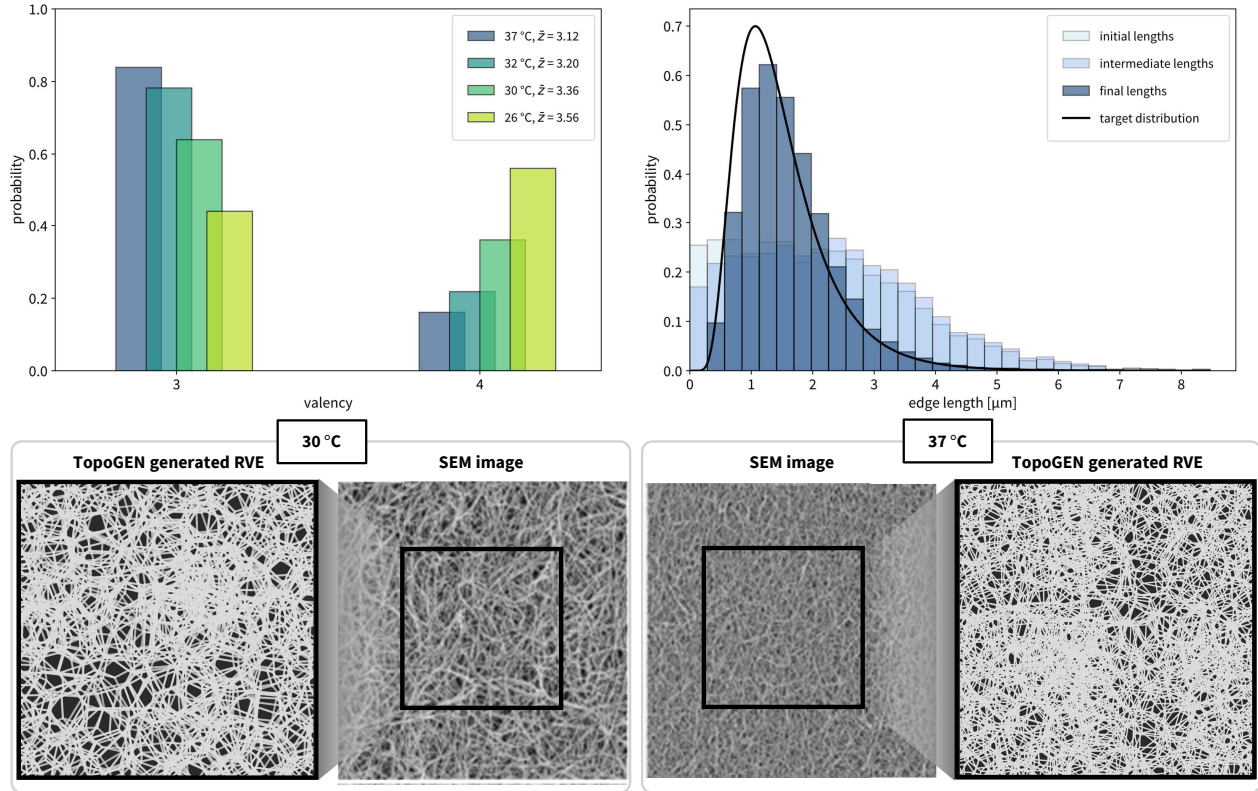


Figure 3: **TopoGEN in action, experimentally informed discrete fiber network topology optimization.** The top row shows simulated annealing results of the valency and length optimization process for different temperatures. Increasing the temperature decreases the network’s average valency ( $\bar{z}$ ), leading to more branches forming between fibers (left plot). Weighted edge removal facilitates an intermediate optimization stage, where shorter edges are preferentially removed during system dilution. Subsequently, the algorithm shifts the intermediate state toward the final optimized configuration by rearranging the network’s nodes. The length optimization is shown here for the 37 °C condition at a concentration of 4 mg/mL (central plot). The four images on the bottom row compare scanning electron microscopy (SEM) images (*taken from Jansen et al. (2018)*) of reconstituted collagen I network in vitro (central images) with the simulated maximum intensity projection of our three-dimensional in silico reconstructions (external images) at 30 °C and 37 °C, respectively. The black squares in the experimental and simulation images have an edge length of 20  $\mu\text{m}$ .

### 3.2. Boundary value problem at the mesoscale

Figure 4 showcases an exemplary finite element simulation outcome of a representative fiber network generated at 37 °C, with an average valency of 3.12, a concentration of 4 mg/mL, and an average fiber length of 2  $\mu\text{m}$ . The generated RVE undergoes uniaxial, biaxial, and simple shear deformations with fully periodic boundary conditions. We conduct all our RVE mechanical deformation analyses using Abaqus/Standard. To ensure convergence, we adhere to Abaqus’ default convergence criteria and employ automatic stabilization. We strictly

require that at every increment, the ratio of viscous damping energy (reported as ALLSD) to total strain energy (reported as ALLSE) does not exceed 2% (Kakaletsis et al., 2023).

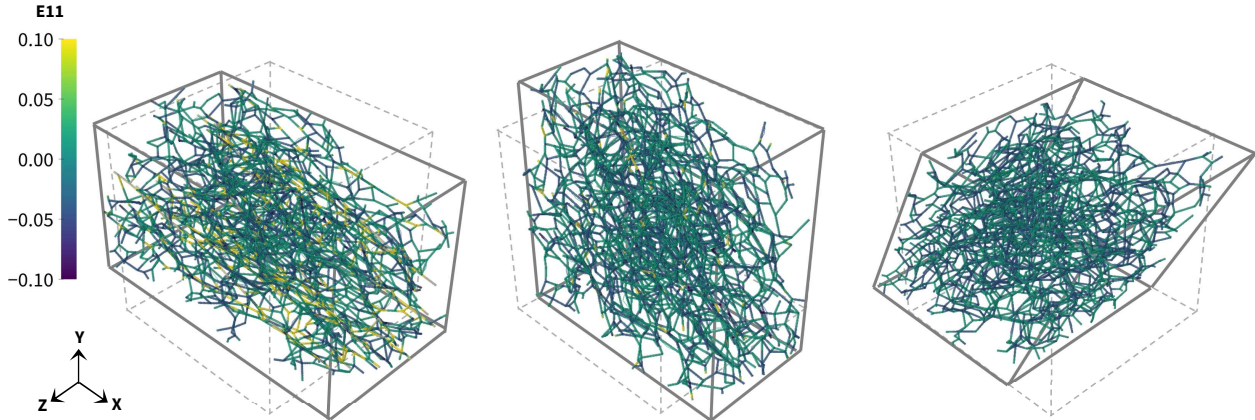
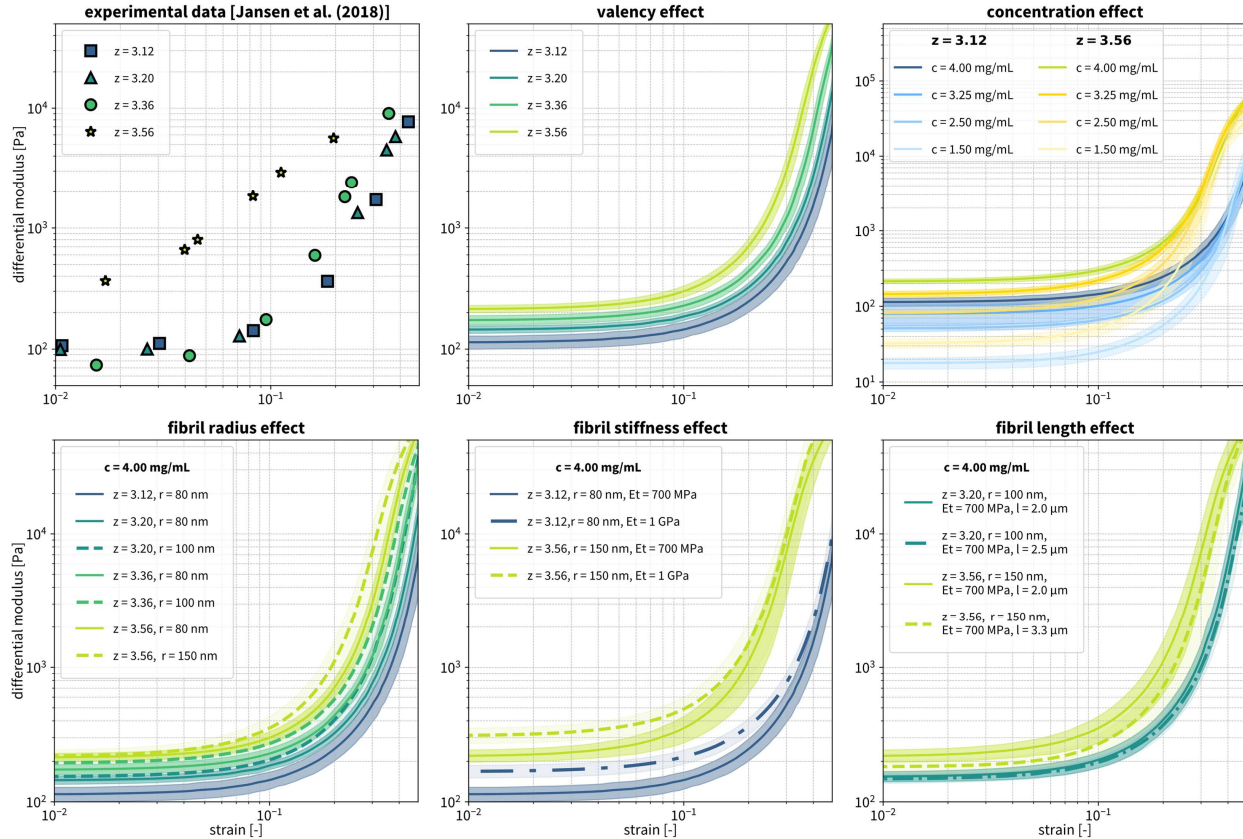


Figure 4: **Multiaxial loading with periodic boundary conditions.** Fiber logarithmic strain distribution in a representative (37 °C, average valency = 3.12, concentration = 4 mg/mL, average fiber length = 2  $\mu$ m) RVE under uniaxial (left), biaxial (middle), and simple shear (right) loading, with 50% strain applied for each loading condition. The undeformed cubic domain is shown with dashed lines and the deformed domain with solid lines.

### 3.3. Microstructure-function relationships in simulated collagen networks

To evaluate how each microstructural feature influences the network’s differential shear modulus, we systematically vary each structural parameter based on experimental observations for collagen type I networks (Table S.1) and perform simple shear tests up to 50% strain on ten representative samples per tested topological or microstructural alteration. We analyze the impact that these topological and microstructural changes have on the differential shear modulus across increasing strain levels relative to the average value of the original network architecture. Figure 5 illustrates the mechanical response for various topological and microstructural parameters derived from experiments and our simulations. We examine the role of additional network-level factors (i.e., valency and concentration) and fibril-level characteristics (i.e., radius, stiffness, and average length) using our 3D simulations. We systematically alter these parameters within the experimentally reported ranges from Jansen et al. (2018) (Table S.1) for diameter and average fiber length, and from Mahutga et al. (2023); Gacek et al. (2023) for fibril stiffness. We find that transitioning from the low-strain to the high-strain regime results in a nonlinear stiffening for all tested topologies. In particular, for all collagen type I networks, we observe a two-order increase in strain stiffening from the initial to the maximum differential shear modulus, with significant stiffening emerging in the medium- to high-strain regime. Our model results are consistent with the experimental data from Jansen et al. (2018) where the concentration is fixed at 4 mg/mL while the average valency is varied based on experimental measurements (Figure 5 - experimental data and valency effect). Conversely, variations in concentration exhibit an uneven impact, with the most significant changes in the differential shear modulus occurring in the low-strain

regime (Figure 5 - concentration effect). In this regime, fibrils primarily undergo non-affine rotations to align with the principal loading direction. Notably, increasing the concentration from 1.5 to 4 mg/mL results in an order-of-magnitude increase in the initial differential shear modulus. In contrast, within the large-strain regime, the maximum modulus remains largely insensitive to concentration changes. At a concentration of 1.5 mg/mL, our models predict an almost three-order-of-magnitude increase in modulus when transitioning from the low- to high-strain regime for both valencies tested.



**Figure 5: Analysis of microstructure-mechanics relationship in reconstituted collagen networks.** The differential shear modulus is shown as a function of strain on a log-log scale for each tested condition. The top row presents (1) experimental results from rheological tests on reconstituted collagen networks with a concentration of 4 mg/mL at varying average valencies (Jansen et al., 2018) and our simulation results from shear tests (up to 50% strain) for (2) 4 mg/mL samples at the same valencies tested experimentally and (3) decreasing concentrations at fixed valencies of 3.12 and 3.56. In all the top row simulations, the fibril-related parameters are set to their minimum values, with fibril radius of 80 nm, Young’s modulus of 700 MPa in tension and 70 MPa in compression, and an average length of 2  $\mu$ m. The bottom row shows simulation results under the same loading conditions as the top row, focusing on the impact of collagen fibril morphology and micromechanics. These results examine inter- and intra-valency effects at a 4 mg/mL fixed concentration. All simulation results represent the response of ten samples per condition, with the average response shown as a line and the standard deviation indicated by the shaded area.

With regard to the morphological changes of the fibers, variations in radius and length

do not exhibit noticeable effects across all tested valencies and strain ranges (Figure 5 - fibril radius and length effects). Overall, increasing the radius slightly increases the network’s differential shear modulus, whereas increasing the length leads to its reduction. This is because longer, more slender fibrils are more susceptible to bending, particularly in the low-strain regime when they are not aligned with the primary loading direction. Increasing Young’s modulus from 700 MPa to 1 GPa (Figure 5 - fibril stiffness effects) yields comparable behavior for the medium-to-high-strain regime. However, it exerts a more pronounced influence in the low-strain regime. Notably, these findings remain consistent across different valency conditions, suggesting that they are independent of the polymerization temperature used to form the network. Table 1 summarizes the deformation-dependent influence of each microstructural parameter on the network’s bulk elastic properties. To build the table, we compare the variation in the differential shear modulus for each microstructural parameter by averaging data from 10 independent samples for each tested condition. At predetermined strain points, we compute the mean and standard deviation for each condition and derive the normalized difference between the means. We aggregate these normalized changes across all parameters and compute the 33<sup>rd</sup> and 67<sup>th</sup> percentiles to set thresholds: values below the 33<sup>rd</sup> percentile indicate a low impact, values between the 33<sup>rd</sup> and 67<sup>th</sup> percentiles indicate a moderate impact, and values above the 67<sup>th</sup> percentile indicate a high impact.

Table 1: Microstructure effect on differential shear modulus across different strain ranges. Symbols  $\approx$ ,  $\uparrow$  /  $\downarrow$ , and  $\uparrow\uparrow$  stand for low, moderate, and high impact, respectively.

strain [-]	0.010	0.125	0.250	0.375	0.500
<b>average valency</b>	$\uparrow\uparrow$	$\uparrow\uparrow$	$\uparrow\uparrow$	$\uparrow\uparrow$	$\uparrow\uparrow$
<b>concentration</b>	$\uparrow\uparrow$	$\uparrow\uparrow$	$\uparrow$	$\approx$	$\approx$
<b>fibrils radius</b>	$\approx$	$\approx$	$\uparrow$	$\approx$	$\approx$
<b>fibrils stiffness</b>	$\uparrow\uparrow$	$\uparrow$	$\uparrow$	$\uparrow$	$\uparrow\uparrow$
<b>fibrils length</b>	$\approx$	$\approx$	$\downarrow$	$\approx$	$\approx$

#### 3.4. Non-affinity in simulated collagen network

Figure 6 illustrates the discrepancy between the nodal displacements predicted by our in silico simulations and the affine predictions based on the deformation gradient imposed at the boundaries. Here, we focus on two specific cases: loosely connected networks with an average valency of  $\bar{z} = 3.12$ , and more interconnected networks with average valency of  $\bar{z} = 3.56$ . We define the non-affinity score ( $NS$ ) as the normalized root mean squared error between purely affine deformation ( $u_{affine}$ ) of the whole network (i.e., the displacements obtained by interpolating the macroscopic deformation gradient imposed at the boundaries to all internal

nodes) and the displacements predicted in our simulations ( $u_{predicted}$ ):

$$NS = \sqrt{\frac{\sum_{i=1}^n \left( u_{predicted}^{(i)} - u_{affine}^{(i)} \right)^2}{\sum_{i=1}^n \left( u_{predicted}^{(i)} - \bar{u}_{predicted} \right)^2}} \quad (4)$$

where  $n$  is the total number of nodes.

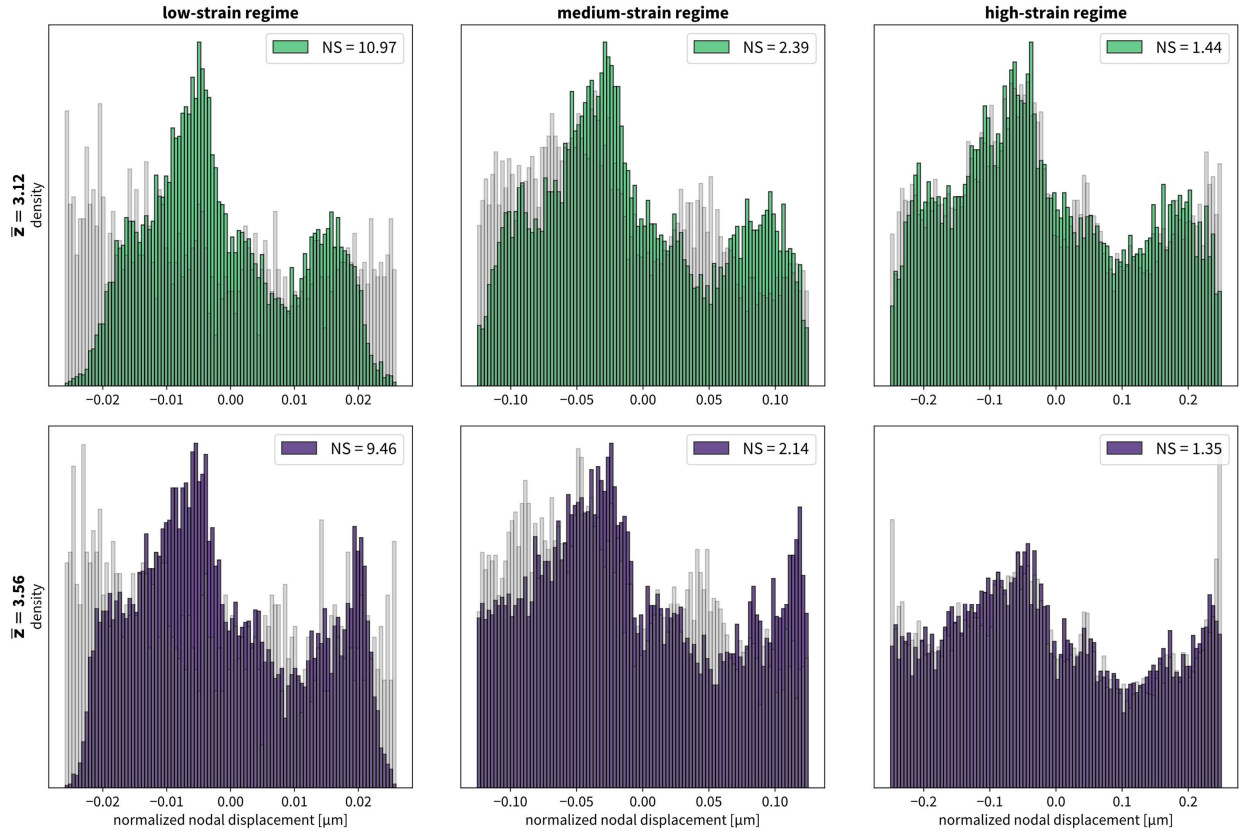


Figure 6: **Non-affinity score with nodal displacements.** Comparison of predicted affine displacements (gray) and computed displacements for five samples, with average valency  $\bar{z} = 3.12$  (top row) and valency  $\bar{z} = 3.56$  (bottom row), at three distinct strain levels. For low-strain regime non-affine modes predominate, with a large set of nodes not following the boundary displacement based on the macroscopic deformation gradient. At strain 0.5, strain-induced affinity enhances the agreement between predicted and measured distributions.

The networks exhibit different behavior from the affine model under all the tested conditions. The most significant discrepancies occur in the low- to medium-strain regime, where the  $NS$  score decreases fivefold. In contrast, the medium- to high-strain regime experiences only a twofold reduction. In the low-strain regime, very few nodes adhere to the boundary displacement prescribed by the imposed macroscopic deformation gradient. However, a noticeable shift occurs in the medium- to high-strain regime, where nodal displacements closely

follow an overall affine displacement pattern. Both loosely connected (with  $\bar{z} = 3.12$ ) and more interconnected (with  $\bar{z} = 3.56$ ) networks converge toward a more affine response at higher strain levels. Networks with lower valency exhibit slightly increased non-affinity in the low-strain regime than those with higher valency. With fewer fibers aligning with the affine deformation, load distribution in these low-valencies, loosely connected networks, becomes highly localized. Increasing the number of cross-links compared to the branches (with  $\bar{z} = 3.56$ ) results in a marginally improved match between the theoretical affine predictions and the experimental measurements. Overall, these sub-static networks exhibit nodal deformation patterns that, in the low- to medium-strain regime, deviate from affine deformation assumptions.

## 4. Discussion

### 4.1. Topological complexity and heterogeneity

Many materials - not just biological materials - are made of fibers. Natural fibrous materials include cotton, wool, and silk, while industrial examples range from polymeric foams and rubber to felt and paper. Among biological materials, an important fibrous system is the extracellular matrix, where collagen fibers assemble into networks to bear mechanical loads and transmit mechanical information over long distances (Ban et al., 2016). Another crucial fibrous system is fibrin, derived from fibrinogen, which assembles into a fibrillar network upon tissue injury to form blood clots. These clots must withstand high tensile forces from blood flow while ensuring rapid degradation after wound healing to prevent thrombosis (Pieters and Wolberg, 2019). Accurately modeling this seemingly passive fibrous environment through computational methods remains a significant challenge. A key requirement is to account for the three-dimensional arrangement of these networks and their structural heterogeneity, which affects the local cellular environment and influences the overall mechanical response of tissues. In this study, we employ a mechanistic approach that explicitly models the interconnected fiber networks underlying soft tissues by leveraging high-resolution imaging data. This framework enables us to investigate how macroscopic material behavior emerges from its microscopic constituents, accounting for microstructural variations. Our generative pipeline builds on the framework by Lindström et al. (2010), where high-resolution confocal images are adopted to derive an image-based representation of collagen networks using simulated annealing. The iterative optimization process is designed to transform initially random Voronoi networks into structures that accurately represent the target biological network in terms of valency and length distribution. Compared to Lindström et al. (2010), we capture the non-affine localized effects by restricting the network to include only cross-links and branches. For the length optimization, we employ Kullback-Leibler divergence to compare the actual and target distributions throughout the iterative optimization process. As a result, we improve the energy accuracy of the optimization process without increasing runtimes compared to the commonly used (Lindström et al., 2010, 2013; Nan et al., 2018; Eichinger et al., 2021a) CVM tests. Notably, while the probabilistic search strategy of simulated annealing cannot

guarantee convergence of the optimization scheme to the global minimum (Suman and Kumar, 2006), it is sufficient for our purposes that the final configuration statistically aligns with experimental measurements without requiring exact correspondence. While focused on collagen-like networks, our modeling pipeline can adapt to other biomaterials and topologies. For instance, we can effectively tune the fibers to replicate the morphology and mechanics of fibrin networks to simulate the mechanical behavior of another essential load-bearing biopolymer in the extracellular space. Alternatively, we can introduce higher valencies by merging nodes within a specific distance threshold, or we can disregard the bending rigidity to model fibers as springs transmitting only central forces, as observed in the intracellular environment of semi-flexible F-actin networks and intermediate filaments (Licup et al., 2015). Leveraging detailed microstructural information, our approach can be extended to model non-living networks. For example, with random Voronoi seeds, we can replicate the microstructure of paper while with regularly arranged seeds, we can create ordered structures, such as those found in fabrics (Picu, 2011).

#### *4.2. Impact of microstructure on stress-strain behavior*

We propose a novel computational approach to systematically analyze how experimentally measured microstructural features affect the nonlinear mechanical properties of the network. To achieve this, we subjected a library of topologically rich and heterogeneous RVEs to shear tests. In constructing the library, we incorporate the experimental evaluations reported by Jansen et al. (2018), wherein temperature variations induce a change in average valency by altering the number of cross-links and branches. Beyond influencing valency, temperature variations also induce morphological changes in the fibers, affecting their average length and diameter. We account for all such microstructural variations and summarize our findings in Table 1. Our results demonstrate that each microstructural parameter exerts a distinct influence on the differential modulus. The network-related parameters exhibit the most pronounced influence on the mechanical response. Specifically, we observe a homogeneous valency effect across the strain range tested, while the concentration effect is particularly prominent in the low-strain regime, consistent with previous findings (Sharma et al., 2016). Regarding fibril effects, the morphology of the fibrils causes only minor overall variations: in the medium-strain regime, a larger fibril radius makes the network stiffer, while a longer fibril softens it. In contrast, the intrinsic stiffness of the fibrils plays a significant role in modulating the variation of the differential modulus, especially in the low-strain regime. These results are important because they allow us to unravel the impact of various microstructural features that are influenced by environmental features such as temperature, concentration, and polymerization, highlighted by Andriotis et al. (2023) to have a crucial impact on the behavior of the collagen network. Indeed, while previous studies have focused on the extraction of network parameters from gels polymerized at different concentrations (Lindström et al., 2010, 2013), experiments show that concentration alone cannot fully characterize the network structure (i.e., mean valency) and the mechanisms of fibril formation (i.e., fibril length, radius, and stiffness). Our work presents a mechanistic approach for modeling discrete fiber networks that explicitly incorporates microstructural variability. This method is

particularly valuable for informing experimental investigations, where the challenge lies in deciphering how individual microstructural features influence the overall mechanical response. This complexity arises from the interplay of multiple multiscale factors, which are difficult to disentangle using typical laboratory protocols. Moreover, because microstructural effects can evolve during rheological loading, typically manifesting as a nonlinear increase in global network stiffness, any comprehensive analysis must account for strain-dependent behavior. Our models thus offer a powerful tool to support experimental assessments of these intricate interactions. In our particular case, we focused on the influence of concentration and temperature, as reported by Jansen et al. (2018), but in the future, we could think of expanding the library by looking at the combined effect of these two parameters or the effect of new environmental parameters, such as pH. For assessing the topology and microstructure effect on differential shear modulus across different strain ranges we assume independence among all the structural parameters. We must underline that this assumption introduces limitations because we disregard the potential existence of confounding factors. Future studies need to systematically isolate confounding factors when analyzing the nonlinear elastic response of collagen or other types of biopolymer networks. Another assumption in our work is that concentration remains constant during polymerization. Advanced imaging could test whether temperature-induced affects fiber volume fraction and provide a clearer understanding of how concentration changes during polymerization. In this work, we focus exclusively on elastic effects, assuming that fiber connections remain permanent with no cross-link breakage. To further enhance the microstructural analysis, future studies should consider time-dependent effects, including the irreversibilities introduced by cross-link breakage.

#### *4.3. Impact of microstructure on non-affinity*

To simulate biopolymer networks polymerized under varying conditions, we optimize random networks with data derived from high-resolution images. While previous studies (Lindström et al., 2010, 2013; Nan et al., 2018; Eichinger et al., 2021a; Mahutga et al., 2023; Leng et al., 2021) treated networks with multiple fibers intersecting at a single node, our model takes a different approach. We exclusively consider fiber-fiber interactions as permanent cross-links or branches, deliberately avoiding higher-order connections that could stabilize the network locally. This choice aligns with the concept of non-affinity that has been increasingly highlighted in recent experimental (Cavinato et al., 2020) and computational (Mahutga et al., 2023; Chen et al., 2023; Parvez and Picu, 2023) works as a crucial factor in understanding local alterations in the extracellular space. Non-affinity arises from the loose interconnections (D’Amore et al., 2010; Burla et al., 2020) between fibers that fall below the Maxwell isostatic threshold (Maxwell, 1864). According to the Maxwell criterion, a three-dimensional central force network is stable only if the average number of fibers per node exceeds six. In isotropic networks, where nodes are branches or cross-links, each branch corresponds to three crossing fibers, and each cross-link corresponds to four. This configuration results in an average number of fibers per node that falls below the Maxwell threshold. In such networks, if the fibers behaved solely as axial load-bearing elements (e.g., springs), the structure would be prone to collapse. However, the structural integrity of networks of stiff filaments - such as collagen



networks - is maintained either through intrinsic stabilizing effects of the fibers (e.g., bending rigidity) or extrinsic factors related to their surrounding environment (e.g., loading conditions). We reflect this principle in our computational model, where stability is ensured by (1) athermal collagen fibrils with a bending-to-stretching stiffness ratio on the order of  $10^{-3}$ , as demonstrated in Licup et al. (2015), and (2) boundary-applied strain, which stabilizes the system by transitioning it from a non-affine to an affine configuration where fibers align with the loading direction and deform consistently with the macroscopic deformation gradient. We define  $NS$  as a metric to quantify the level of non-affinity by measuring the deviation of cross-link displacements obtained from simulations relative to those predicted under a purely affine deformation assumption. The outcome of this score is consistent with previous studies (Broedersz et al., 2011; Sharma et al., 2016), which demonstrate that non-affinity decreases with increasing average valency and applied strain. Additionally, the inconsistency between microscopic and macroscopic affine displacements is most evident at the strain extremes in the low-strain regime for both tested valencies. In this regime, theoretical models predict a more uniform load distribution across the network. This observation confirms that biological networks adopt a highly heterogeneous load distribution strategy and align with previous works (Chandran and Barocas, 2005; Cavinato et al., 2020; Mahutga et al., 2023). This loading heterogeneity is most pronounced during the low-to-medium-strain regime, where most of the fibers rotate or bend while just a few actually stretch. With these findings, we highlight the importance of heterogeneous three-dimensional models in accurately capturing localized phenomena in the space surrounding cells and provide an in-depth insight into the mechanisms of gradual fiber recruitment.

#### *4.4. Untangling the network puzzle*

We examine the influence of the microstructure on the shear differential modulus of collagen networks polymerized at various temperatures. Overall, for all the tested conditions, our analysis highlights a typical three-phase response in discrete fiber networks under load. In the linear elastic phase, the differential modulus remains constant as strain increases, and geometric nonlinearity is negligible. This is followed by the nonlinear stiffening phase, where fibers reorient along the loading direction. A subset of fibers, initially oriented perpendicularly, undergoes significant bending. This geometrically induced nonlinearity happens when non-affine, bending-dominated deformation modes develop. Finally, the stress-strain curve becomes linear in the affine-dominated phase. In this region, stress paths form through fiber chains that connect the boundary faces and limit further structural changes. Our results from the valency effect tests show trends consistent with in vitro rheological tests (Jansen et al., 2018), demonstrating a two-decade increase in stiffness from the initial to the final strain. However, the valency effect alone does not fully account for the observed phenomena. Specifically, networks with higher valency exhibited stiffer responses at low strains and a less pronounced nonlinear effect at higher strains in vitro. Yet, in our computational models and those of Jansen et al. (2018), higher valency networks exhibit nonlinear stiffening patterns that align more closely with those observed in lower valency networks. This suggests that nonlinear elastic behaviors in networks polymerized at different temperatures cannot be fully

explained by valency alone. Our results in Figure 5 highlight the impact that fibril-related parameters such as length, fibril radius, and stiffness have. Another study (Davoodi Kermani et al., 2021) explored the effect of varying morphological and graph descriptors on the linear elastic modulus of different networks. While providing valuable insights, it lacks direct applicability to biological networks subjected to varying environmental conditions and shear loads, resulting in highly nonlinear stress buildup in rheological experiments. In our work, we focus solely on experimentally relevant microstructural variations (as summarized in Table S.1) and evaluate the differential modulus as a function of strain. We propose a novel approach to modeling biologically reconstituted networks that strategically incorporates the variations introduced by polymerization conditions during their reconstruction. In parallel, this approach can also address tissue-specific variations in microstructures observed in-vivo, where other environmental factors can lead to localized changes in the microstructure that result in different mechanical responses. In both cases, it is essential to consider additional structural and topological features to untangle the network puzzle fully. We should direct significant efforts toward extracting detailed network topologies from high-resolution images captured under varying polymerization conditions. Doing so can enrich our models with robust statistical structural variations and provide deeper insights into the structure-to-mechanics relationship across multiple scales.

## 5. Conclusion

Our study provides a detailed analysis of the effects of topology and microstructure on the nonlinear differential shear modulus of biological networks. Without loss of generality for other biological and non-biological fiber networks, we use our developed framework to replicate the subisostatic microstructural architectures typical of collagen networks, enabling a quantitative evaluation of localized non-affine phenomena within these complex three-dimensional environments. We achieve this condition by optimizing the average valency of in silico networks virtually replicating the temperature modification effect on the topology. Additionally, we expand the range of studied conditions by assessing other microstructural features beyond valency. Specifically, we demonstrate that fiber morphology, mechanics, and concentration influence network mechanics across different deformation regimes. For instance, fibril stiffness and concentration have a more significant impact on the low-deformation regime. In contrast, fibril length and diameter play a more significant role in the medium-deformation regime. By aligning our computational models with experimentally derived microstructural characteristics, we propose a generative pipeline that, while rooted in network theory, is foremost designed for experimental application. This pipeline focuses solely on structural parameters that can be experimentally controlled and will benefit from further investigations into how topology changes under varying environmental conditions and, consequently, how these changes affect mechanical responses.

## **CRedit authorship contribution statement**

**Sara Cardona:** Writing – original draft, Methodology, Investigation, Visualization, Validation, Software, Data curation, Conceptualization **Mathias Peirlinck and Behrooz Ferdoonzad:** Writing – review & editing, Resources, Methodology, Investigation, Data curation, Conceptualization.

## **Declaration of competing interest**

The authors declare that they have no known competing financial interests or personal relationships that could have appeared to influence the work reported in this paper.

## **Acknowledgement**

This work was supported by the Delft University of Technology Startup Grant awarded to MP and BF. The authors thank Prof. F.Gijsen (Delft University of Technology, the Netherlands) and Prof. G. Koenderink (Delft University of Technology, the Netherlands) for many useful discussions.

## **References**

- Andriotis, O.G., Nalbach, M., Thurner, P.J., 2023. Mechanics of isolated individual collagen fibrils. *Acta Biomaterialia* 163, 35–49. doi:10.1016/j.actbio.2022.12.008.
- Atcha, H., Choi, Y.S., Chaudhuri, O., Engler, A.J., 2023. Getting physical: Material mechanics is an intrinsic cell cue. *Cell Stem Cell* 30, 750–765. doi:10.1016/j.stem.2023.05.003.
- Ayad, N.M.E., Kaushik, S., Weaver, V.M., 2019. Tissue mechanics, an important regulator of development and disease. *Philosophical Transactions of the Royal Society B: Biological Sciences* 374, 20180215. doi:10.1098/rstb.2018.0215.
- Ban, E., Barocas, V.H., Shephard, M.S., Picu, C.R., 2016. Effect of fiber crimp on the elasticity of random fiber networks with and without embedding matrices. *Journal of Applied Mechanics* 83. doi:10.1115/1.4032465.
- Ban, E., Wang, H., Franklin, J.M., Liphardt, J.T., Janmey, P.A., Shenoy, V.B., 2019. Strong triaxial coupling and anomalous poisson effect in collagen networks. *Proceedings of the National Academy of Sciences* 116, 6790–6799. doi:10.1073/pnas.1815659116.
- Broedersz, C.P., Mao, X., Lubensky, T.C., MacKintosh, F.C., 2011. Criticality and isostaticity in fibre networks. *Nature Physics* 7, 983–988. doi:10.1038/nphys2127.
- Burla, F., Dussi, S., Martinez-Torres, C., Tauber, J., van der Gucht, J., Koenderink, G.H., 2020. Connectivity and plasticity determine collagen network fracture. *Proceedings of the National Academy of Sciences* 117, 8326–8334. doi:10.1073/pnas.1920062117.

- Burla, F., Mulla, Y., Vos, B.E., Aufderhorst-Roberts, A., Koenderink, G.H., 2019a. From mechanical resilience to active material properties in biopolymer networks. *Nature Reviews Physics* 1, 249–263. doi:10.1038/s42254-019-0036-4.
- Burla, F., Tauber, J., Dussi, S., van der Gucht, J., Koenderink, G.H., 2019b. Stress management in composite biopolymer networks. *Nature Physics* 15, 549–553. doi:10.1038/s41567-019-0443-6.
- Buskermolen, A.B., Ristori, T., Mostert, D., van Turnhout, M.C., Shishvan, S.S., Loerakker, S., Kurniawan, N.A., Deshpande, V.S., Bouten, C.V., 2020. Cellular contact guidance emerges from gap avoidance. *Cell Reports Physical Science* 1, 100055. doi:10.1016/j.xcrp.2020.100055.
- Cavinato, C., Badel, P., Krasny, W., Avril, S., Morin, C., 2020. Experimental Characterization of Adventitial Collagen Fiber Kinematics Using Second-Harmonic Generation Imaging Microscopy: Similarities and Differences Across Arteries, Species and Testing Conditions. Springer International Publishing, Cham. doi:10.1007/978-3-030-20182-1\_5.
- Chandran, P.L., Barocas, V.H., 2005. Affine versus non-affine fibril kinematics in collagen networks: Theoretical studies of network behavior. *Journal of Biomechanical Engineering* 128, 259–270. doi:10.1115/1.2165699.
- Chen, S., Markovich, T., MacKintosh, F.C., 2023. Nonaffine deformation of semiflexible polymer and fiber networks. *Physical Review Letters* 130, 088101. doi:10.1103/physrevlett.130.088101.
- Dalbosco, M., Carniel, T.A., Fancello, E.A., Holzapfel, G.A., 2021. Multiscale numerical analyses of arterial tissue with embedded elements in the finite strain regime. *Computer Methods in Applied Mechanics and Engineering* 381, 113844. doi:10.1016/j.cma.2021.113844.
- Dassault Systèmes Simulia Corp., 2024. Abaqus analysis user’s guide. Dassault Systèmes Simulia Corp., Providence.
- Davoodi Kermani, I., Schmitter, M., Eichinger, J.F., Aydin, R.C., Cyron, C.J., 2021. Computational study of the geometric properties governing the linear mechanical behavior of fiber networks. *Computational Materials Science* 199, 110711. doi:10.1016/j.commatsci.2021.110711.
- Dean, D., Nain, A.S., Genin, G.M., 2023. Special issue: Mechanics of cells and fibers. *Acta Biomaterialia* 163, 1–6. doi:10.1016/j.actbio.2023.04.045.
- D’Amore, A., Stella, J.A., Wagner, W.R., Sacks, M.S., 2010. Characterization of the complete fiber network topology of planar fibrous tissues and scaffolds. *Biomaterials* 31, 5345–5354. doi:10.1016/j.biomaterials.2010.03.052.

- Eichinger, J.F., Grill, M.J., Kermani, I.D., Aydin, R.C., Wall, W.A., Humphrey, J.D., Cyron, C.J., 2021a. A computational framework for modeling cell–matrix interactions in soft biological tissues. *Biomechanics and Modeling in Mechanobiology* 20, 1851–1870. doi:10.1007/s10237-021-01480-2.
- Eichinger, J.F., Haeusel, L.J., Paukner, D., Aydin, R.C., Humphrey, J.D., Cyron, C.J., 2021b. Mechanical homeostasis in tissue equivalents: a review. *Biomechanics and Modeling in Mechanobiology* 20, 833–850. doi:10.1007/s10237-021-01433-9.
- Espina, J.A., Marchant, C.L., Barriga, E.H., 2021. Durotaxis: the mechanical control of directed cell migration. *The FEBS Journal* 289, 2736–2754. doi:10.1111/febs.15862.
- Fereidoonzezhad, B., Naghdabadi, R., Sohrabpour, S., Holzapfel, G., 2017. A mechanobiological model for damage-induced growth in arterial tissue with application to in-stent restenosis. *Journal of the Mechanics and Physics of Solids* 101, 311–327. doi:10.1016/j.jmps.2017.01.016.
- Filla, N., Hou, J., Li, H., Wang, X., 2023. A multiscale framework for modeling fibrin fiber networks: Theory development and validation. *Journal of the Mechanics and Physics of Solids* 179, 105392. doi:10.1016/j.jmps.2023.105392.
- Fung, Y., 1967. Elasticity of soft tissues in simple elongation. *American Journal of Physiology-Legacy Content* 213, 1532–1544. doi:10.1152/ajplegacy.1967.213.6.1532.
- Gacek, E., Mahutga, R.R., Barocas, V.H., 2023. Hybrid discrete-continuum multiscale model of tissue growth and remodeling. *Acta Biomaterialia* 163, 7–24. doi:10.1016/j.actbio.2022.09.040.
- Gasser, T.C., Ogden, R.W., Holzapfel, G.A., 2005. Hyperelastic modelling of arterial layers with distributed collagen fibre orientations. *Journal of The Royal Society Interface* 3, 15–35. doi:10.1098/rsif.2005.0073.
- Geers, M., Kouznetsova, V., Brekelmans, W., 2010. Multi-scale computational homogenization: Trends and challenges. *Journal of Computational and Applied Mathematics* 234, 2175–2182. doi:10.1016/j.cam.2009.08.077.
- Herum, K.M., Choppe, J., Kumar, A., Engler, A.J., McCulloch, A.D., 2017. Mechanical regulation of cardiac fibroblast profibrotic phenotypes. *Molecular Biology of the Cell* 28, 1871–1882. doi:10.1091/mbc.e17-01-0014.
- Hill, R., 1963. Elastic properties of reinforced solids: Some theoretical principles. *Journal of the Mechanics and Physics of Solids* 11, 357–372. doi:10.1016/0022-5096(63)90036-x.
- Holzapfel, G.A., Gasser, T.C., Ogden, R.W., 2000. A new constitutive framework for arterial wall mechanics and a comparative study of material models. *Journal of Elasticity* 61, 1–48. doi:10.1023/a:1010835316564.

- Hulmes, D.J.S., Miller, A., 1979. Quasi-hexagonal molecular packing in collagen fibrils. *Nature* 282, 878–880. doi:10.1038/282878a0.
- Jansen, K.A., Donato, D.M., Balcioglu, H.E., Schmidt, T., Danen, E.H., Koenderink, G.H., 2015. A guide to mechanobiology: Where biology and physics meet. *Biochimica et Biophysica Acta (BBA) - Molecular Cell Research* 1853, 3043–3052. doi:10.1016/j.bbamcr.2015.05.007.
- Jansen, K.A., Licup, A.J., Sharma, A., Rens, R., MacKintosh, F.C., Koenderink, G.H., 2018. The role of network architecture in collagen mechanics. *Biophysical Journal* 114, 2665–2678. doi:10.1016/j.bpj.2018.04.043.
- Kakaletsis, S., Lejeune, E., Rausch, M., 2023. The mechanics of embedded fiber networks. *Journal of the Mechanics and Physics of Solids* 181, 105456. doi:10.1016/j.jmps.2023.105456.
- Kanit, T., N’Guyen, F., Forest, S., Jeulin, D., Reed, M., Singleton, S., 2006. Apparent and effective physical properties of heterogeneous materials: Representativity of samples of two materials from food industry. *Computer Methods in Applied Mechanics and Engineering* 195, 3960–3982. doi:10.1016/j.cma.2005.07.022.
- Kim, S., Uroz, M., Bays, J.L., Chen, C.S., 2021. Harnessing mechanobiology for tissue engineering. *Developmental Cell* 56, 180–191. doi:10.1016/j.devcel.2020.12.017.
- Kullback, S., Leibler, R.A., 1951. On information and sufficiency. *The Annals of Mathematical Statistics* 22, 79–86. doi:10.1214/aoms/1177729694.
- Kumar, V., Naqvi, S.M., Verbruggen, A., McEvoy, E., McNamara, L.M., 2024. A mechanobiological model of bone metastasis reveals that mechanical stimulation inhibits the pro-osteolytic effects of breast cancer cells. *Cell Reports* 43, 114043. doi:10.1016/j.celrep.2024.114043.
- Leng, Y., Tac, V., Calve, S., Tepole, A.B., 2021. Predicting the mechanical properties of biopolymer gels using neural networks trained on discrete fiber network data. *Computer Methods in Applied Mechanics and Engineering* 387, 114160. doi:10.1016/j.cma.2021.114160.
- Licup, A.J., Münster, S., Sharma, A., Sheinman, M., Jawerth, L.M., Fabry, B., Weitz, D.A., MacKintosh, F.C., 2015. Stress controls the mechanics of collagen networks. *Proceedings of the National Academy of Sciences* 112, 9573–9578. doi:10.1073/pnas.1504258112.
- Lindström, S.B., Kulachenko, A., Jawerth, L.M., Vader, D.A., 2013. Finite-strain, finite-size mechanics of rigidly cross-linked biopolymer networks. *Soft Matter* 9, 7302. doi:10.1039/c3sm50451d.

- Lindström, S.B., Vader, D.A., Kulachenko, A., Weitz, D.A., 2010. Biopolymer network geometries: Characterization, regeneration, and elastic properties. *Physical Review E* 82, 051905. doi:10.1103/physreve.82.051905.
- Loerakker, S., Humphrey, J.D., 2022. Computer model-driven design in cardiovascular regenerative medicine. *Annals of Biomedical Engineering* 51, 45–57. doi:10.1007/s10439-022-03037-5.
- Mahutga, R.R., Barocas, V.H., Alford, P.W., 2023. The non-affine fiber network solver: A multiscale fiber network material model for finite-element analysis. *Journal of the Mechanical Behavior of Biomedical Materials* 144, 105967. doi:10.1016/j.jmbbm.2023.105967.
- Maxwell, J.C., 1864. L. on the calculation of the equilibrium and stiffness of frames. *The London, Edinburgh, and Dublin Philosophical Magazine and Journal of Science* 27, 294–299. doi:10.1080/14786446408643668.
- McEvoy, E., McNamara, L., 2024. *Mechanobiology regulation*. Elsevier. doi:10.1016/b978-0-323-91821-3.00007-4.
- Merson, J., Picu, R., 2020. Size effects in random fiber networks controlled by the use of generalized boundary conditions. *International Journal of Solids and Structures* 206, 314–321. doi:10.1016/j.ijsolstr.2020.09.033.
- Miehe, C., Koch, A., 2002. Computational micro-to-macro transitions of discretized microstructures undergoing small strains. *Archive of Applied Mechanics (Ingenieur Archiv)* 72, 300–317. doi:10.1007/s00419-002-0212-2.
- Mirzaali, M.J., Pahlavani, H., Yarali, E., Zadpoor, A.A., 2020. Non-affinity in multi-material mechanical metamaterials. *Scientific Reports* 10. doi:10.1038/s41598-020-67984-6.
- Nan, H., Liang, L., Chen, G., Liu, L., Liu, R., Jiao, Y., 2018. Realizations of highly heterogeneous collagen networks via stochastic reconstruction for micromechanical analysis of tumor cell invasion. *Physical Review E* 97, 033311. doi:10.1103/physreve.97.033311.
- Nikpasand, M., Mahutga, R.R., Bersie-Larson, L.M., Gacek, E., Barocas, V.H., 2021. A hybrid microstructural-continuum multiscale approach for modeling hyperelastic fibrous soft tissue. *Journal of Elasticity* 145, 295–319. doi:10.1007/s10659-021-09843-7.
- Notbohm, J., Lesman, A., Rosakis, P., Tirrell, D.A., Ravichandran, G., 2015. Microbuckling of fibrin provides a mechanism for cell mechanosensing. *Journal of The Royal Society Interface* 12, 20150320. doi:10.1098/rsif.2015.0320.
- Parvez, N., Picu, C.R., 2023. Effect of connectivity on the elasticity of athermal network materials. *Soft Matter* 19, 106–114. doi:10.1039/d2sm01303g.

- Peirlinck, M., Hurtado, J.A., Rausch, M.K., Tepole, A.B., Kuhl, E., 2024. A universal material model subroutine for soft matter systems. *Engineering with Computers* doi:10.1007/s00366-024-02031-w.
- Peirlinck, M., Sahli Costabal, F., Sack, K.L., Choy, J.S., Kassab, G.S., Guccione, J.M., De Beule, M., Segers, P., Kuhl, E., 2019. Using machine learning to characterize heart failure across the scales. *Biomechanics and Modeling in Mechanobiology* 18, 1987–2001. doi:10.1007/s10237-019-01190-w.
- Perić, D., de Souza Neto, E.A., Feijóo, R.A., Partovi, M., Molina, A.J.C., 2010. On micro-to-macro transitions for multi-scale analysis of non-linear heterogeneous materials: unified variational basis and finite element implementation. *International Journal for Numerical Methods in Engineering* 87, 149–170. doi:10.1002/nme.3014.
- Picu, R.C., 2011. Mechanics of random fiber networks—a review. *Soft Matter* 7, 6768. doi:10.1039/c1sm05022b.
- Pieters, M., Wolberg, A.S., 2019. Fibrinogen and fibrin: An illustrated review. *Research and Practice in Thrombosis and Haemostasis* 3, 161–172. doi:10.1002/rth2.12191.
- van Putten, S., Shafieyan, Y., Hinz, B., 2016. Mechanical control of cardiac myofibroblasts. *Journal of Molecular and Cellular Cardiology* 93, 133–142. doi:10.1016/j.yjmcc.2015.11.025.
- Shahsavari, A., Picu, R., 2013. Size effect on mechanical behavior of random fiber networks. *International Journal of Solids and Structures* 50, 3332–3338. doi:10.1016/j.ijsolstr.2013.06.004.
- Shahsavari, A., Picu, R.C., 2012. Model selection for athermal cross-linked fiber networks. *Physical Review E* 86, 011923. doi:10.1103/physreve.86.011923.
- Sharma, A., Licup, A.J., Jansen, K.A., Rens, R., Sheinman, M., Koenderink, G.H., MacKintosh, F., 2016. Strain-controlled criticality governs the nonlinear mechanics of fibre networks. *Nature Physics* 12, 584–587. doi:10.1038/nphys3628.
- van der Sluis, O., Schreurs, P., Brekelmans, W., Meijer, H., 2000. Overall behaviour of heterogeneous elastoviscoplastic materials: effect of microstructural modelling. *Mechanics of Materials* 32, 449–462. doi:10.1016/s0167-6636(00)00019-3.
- Suman, B., Kumar, P., 2006. A survey of simulated annealing as a tool for single and multiobjective optimization. *Journal of the Operational Research Society* 57, 1143–1160. doi:10.1057/palgrave.jors.2602068.
- Terada, K., Hori, M., Kyoya, T., Kikuchi, N., 2000. Simulation of the multi-scale convergence in computational homogenization approaches. *International Journal of Solids and Structures* 37, 2285–2311. doi:10.1016/s0020-7683(98)00341-2.



Wahlsten, A., Stracuzzi, A., Lüchtfeld, I., Restivo, G., Lindenblatt, N., Giampietro, C., Ehret, A.E., Mazza, E., 2023. Multiscale mechanical analysis of the elastic modulus of skin. *Acta Biomaterialia* 170, 155–168. doi:10.1016/j.actbio.2023.08.030.

Wu, W., Owino, J., Al-Ostaz, A., Cai, L., 2014. Applying periodic boundary conditions in finite element analysis, in: SIMULIA community conference, Providence, pp. 707–719.

Yeong, C.L.Y., Torquato, S., 1998. Reconstructing random media. *Physical Review E* 57, 495–506. doi:10.1103/physreve.57.495.

## 6. Supplemental Information

### 6.1. Collagen network and fibrils properties based on experiments

Table S.1: Network properties of collagen type I at 4 mg/mL concentration across varying polymerization temperatures (Jansen et al., 2018)

Property	Temperature	Experimental observations
<b>Network appearance</b> ( <i>Confocal reflectance microscopy</i> )	22°C	Very heterogeneous, open structure with fan-shaped bundles of fibrils.
	26°C	Heterogeneous, open structure with bundles of fibrils. More uniform bundle width compared to 22°C.
	30–37°C	Dense, isotropic, and uniform.
<b>Fibrils diameter</b> ( <i>Scanning electron microscopy (SEM) and Light scattering (LS)</i> )	22°C	<i>SEM</i> : Not quantified due to open fan-shaped bundles of fibrils. <i>LS</i> : Thickest fibrils with an average diameter of 300 nm.
	26–30°C	<i>SEM</i> : 150 nm on average, with significant spread at 26°C. <i>LS</i> : Comparable diameters of approximately 200 nm.
	34–37°C	<i>SEM</i> : Consistent diameter around 70 nm. <i>LS</i> : Smaller diameters of approximately 150 nm.
<b>Fibrils length</b> ( <i>Light scattering</i> )	26–37°C	Reduces from 3.3 $\mu\text{m}$ at 26°C to 1.6 $\mu\text{m}$ at 37°C.

### 6.2. Comparative analysis of Kullback–Leibler (KL) divergence and the Cramér–von Mises (CVM) test

To compare the energy computation of CVM with that of KL, we examine runtime and percentage improvement for the two tests across varying connectivity values ( $z$ ). The runtime

for both methods is generally comparable, with CVM marginally outperforming KL in several cases. KL regularly shows larger percentage improvements suggesting more efficiency. The Wasserstein distance (Wass.) is presented as an extra statistic. Overall, KL outperforms CVM in terms of percentage improvement.

Table S.2: Runtime, Improvement Percentage, and Wasserstein Distance: CVM vs KL

Test	z	CVM Metrics			KL Metrics		
		Runtime (s)	% Improvement	Wass.	Runtime (s)	% Improvement	Wass.
1	3.12	32.07	97.53	0.0043	32.35	98.82	0.0033
2	3.12	34.89	91.29	0.0044	35.12	99.42	0.0033
3	3.12	30.43	87.01	0.0044	33.80	99.65	0.0033
4	3.12	32.38	85.64	0.0042	34.76	98.85	0.0043
5	3.12	29.21	85.58	0.0037	32.07	99.58	0.0026
6	3.20	34.64	95.90	0.0066	30.35	99.15	0.0046
7	3.20	35.81	95.69	0.0058	38.30	97.00	0.0042
8	3.20	32.77	87.69	0.0068	37.91	99.30	0.0055
9	3.20	31.91	96.84	0.0064	31.85	99.32	0.0050
10	3.20	34.43	97.44	0.0058	37.08	99.38	0.0057
11	3.36	32.93	90.63	0.0097	30.33	97.24	0.0067
12	3.36	34.92	89.69	0.0062	37.27	98.74	0.0053
13	3.36	31.02	92.83	0.0090	33.83	97.39	0.0059
14	3.36	31.63	77.34	0.0090	30.76	94.70	0.0077
15	3.36	33.74	86.82	0.0067	30.36	98.69	0.0066
16	3.56	30.13	83.92	0.0124	34.25	96.84	0.0095
17	3.56	37.51	77.87	0.0115	30.34	96.22	0.0099
18	3.56	34.79	85.38	0.0098	35.87	94.90	0.0095
19	3.56	32.04	84.11	0.0101	34.58	97.27	0.0091
20	3.56	31.06	82.93	0.0104	31.11	95.28	0.0103

### 6.3. Influence of topology on differential modulus

The first row of plots shows the network-related analysis, with the first plot comparing valencies of 3.12 and 3.56. For the second plot, the valency is 3.56, and the concentration varies from 4 mg/mL to 1.5 mg/mL. In all remaining plots, we keep valency (3.56) and concentration (4 mg/mL) and examine the effects of collagen fibril morphology and micromechanics.

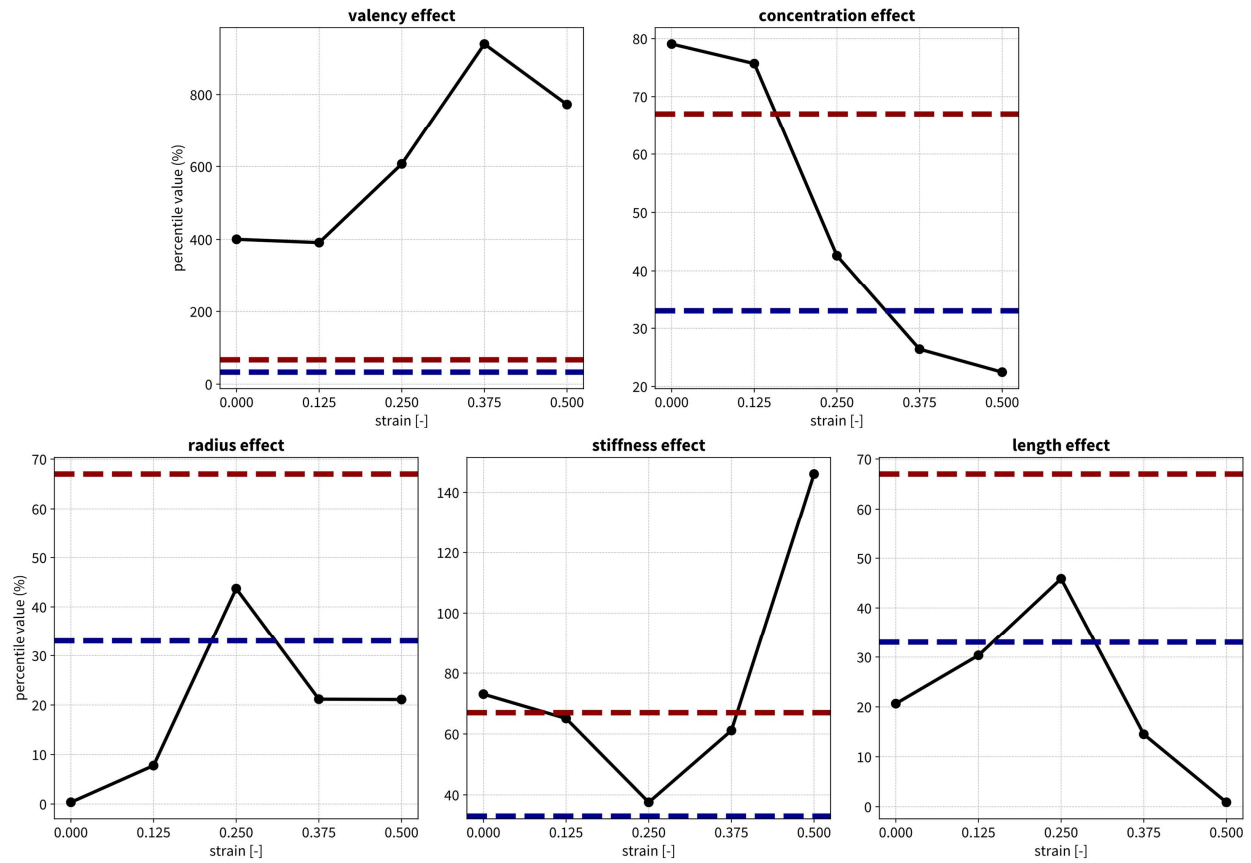


Figure S.1: **Differential modulus variation for different topologies across increasing strain levels.** The first row of plots shows the network-related analysis, with the first plot comparing valencies of 3.12 and 3.56. For the second plot, the valency is 3.56, and the concentration varies from 4 mg/mL to 1.5 mg/mL. In all remaining plots, we keep valency (3.56) and concentration (4 mg/mL) and examine the effects of collagen fibril morphology and micromechanics. For all the plots, the dark blue dashed line represents the low impact threshold (below the 33<sup>rd</sup> percentile), while the dark red dashed line marks the high impact threshold (above the 67<sup>th</sup> percentile). Values falling between these thresholds indicate a moderate impact.